JGR Space Physics

RESEARCH ARTICLE
10.1029/2024JA033096

Complex Ionospheric Fluctuations Over East and Southeast Asia During the May 2024 Super Geomagnetic Storm

Wenjie Sun[1,2], Guozhu Li[1,2,3], Shun-Rong Zhang[4], Biqiang Zhao[1,2,3], Yu Li[5], M. Arslan Tariq[6], Xiukuan Zhao[2,7], Lianhuan Hu[1,2], Guofeng Dai[1,2], Haiyong Xie[1,2,3], Yi Li[1,2], Jianfei Liu[1,2], Baiqi Ning[1,2], and Libo Liu[2,3,7]

[1]Beijing National Observatory of Space Environment, Institute of Geology and Geophysics, Chinese Academy of Sciences, Beijing, China, [2]Key Laboratory of Earth and Planetary Physics, Institute of Geology and Geophysics, Chinese Academy of Sciences, Beijing, China, [3]College of Earth and Planetary Sciences, University of Chinese Academy of Sciences, Beijing, China, [4]Haystack Observatory, Massachusetts Institute of Technology, Westford, MA, USA, [5]China Earthquake Networks Center, China Earthquake Administration, Beijing, China, [6]Centre for Earthquake Studies, National Centre for Physics, Islamabad, Pakistan, [7]Heilongjiang Mohe National Observatory of Geophysics, Institute of Geology and Geophysics, Chinese Academy of Sciences, Beijing, China

Key Points:

- Complex ionospheric fluctuations consisting of poleward extending and equatorward traveling disturbances were identified during super geomagnetic storm
- The poleward oscillations were synchronized over a wide longitude and driven by multiple penetrations of electric fields
- The equatorward traveling disturbances likely occurred around the globe that could be due to auroral energy input

Correspondence to:
G. Li,
gzlee@mail.iggcas.ac.cn

Citation:
Sun, W., Li, G., Zhang, S.-R., Zhao, B., Li, Y., Tariq, M. A., et al. (2024). Complex ionospheric fluctuations over East and Southeast Asia during the May 2024 super geomagnetic storm. *Journal of Geophysical Research: Space Physics*, *129*, e2024JA033096. https://doi.org/10.1029/2024JA033096

Received 22 JUL 2024
Accepted 14 DEC 2024

Abstract The May 2024 super storm is one of the strongest geomagnetic storms during the past 20 years. One of the most remarkable ionospheric responses to this event over East and Southeast Asia is the complex ionospheric fluctuations following the storm commencement. The fluctuations created multiple oscillations of total electron content (TEC) embedded in the diurnal variation, with amplitudes up to 10 TECu. Along the same latitude, the fluctuations were nearly synchronized over a wide longitude span up to 35°. In the meridional direction, the fluctuations over low latitudes were the most significant and complex, which contained two main components, the poleward extending oscillations originated from the magnetic equator, and the equatorward propagating traveling ionospheric disturbances (TIDs) from high latitudes. The TIDs likely occurred around the globe. The storm-time interplanetary electric fields penetrating into equatorial latitudes of the ionosphere and the auroral energy input were suggested to drive the poleward extending oscillations and the equatorward TIDs, respectively.

Plain Language Summary The ionospheric responses to strong geomagnetic storms are mainly in the form of global or hemispheric scale plasma density enhancement or suppression, termed as positive or negative ionospheric storms, respectively. Previous studies have also reported fine-scale ionospheric structures during geomagnetic storms, which were manifested as wavelike fluctuations in TEC. Multiple mechanisms were proposed to be responsible for the TEC fluctuations, including the magnetospheric compression effect, storm-time penetration electric field, refilling process linked with plasma pressure, and traveling ionospheric disturbances triggered from high latitude and polar regions. During the May 2024 super storm, complex ionospheric fluctuations consisting of two major components, that is, poleward extending fluctuations originated from the magnetic equator and equatorward traveling oscillations from high latitude and polar regions were observed over East and Southeast Asia. It is important to figure out what mechanisms could dominate the generation and evolution of complex fluctuations over specific regions. Based on the TEC continuously measured along dense observational chains, in combination with multiple other types of observations, the characteristics and possible mechanisms of the complex ionospheric fluctuations are investigated.

1. Introduction

The Earth's ionosphere could change significantly during strong geomagnetic storms. Due to the variation of equatorial electric fields, thermospheric composition, neutral circulation, and/or auroral energy input during different storm phases, the plasma density may experience remarkable enhancement or suppression, termed as positive or negative ionospheric storms, respectively (e.g., Abdu, 1997; Huang, 2008; Kelley et al., 2003; Kuai et al., 2015; Lei et al., 2011; Prölss, 1993; Spogli et al., 2021; Zhao et al., 2008). The positive and negative ionospheric storms are important space weather events that usually draw the great attention of researchers, and have been extensively investigated during the past decades (e.g., Balan et al., 2010; Fejer, 2002; Lu et al., 2008; Nava et al., 2016; Prölss & Werner, 2002; Zhang et al., 2017; Zhao et al., 2012).

In addition to positive and negative storm effects that usually have global or hemispheric scales, the ionosphere may also experience regional or fine-scale variations during geomagnetic storms. For example, during the March 1989 super geomagnetic storm, it is reported that the ionospheric response over East Asia exhibited significant east-west differences at middle latitude (Zhao et al., 2019), whereas at low latitude the ionospheric total electron content (TEC) displayed fine-scale wavelike disturbances over time, which was surmised to be linked with the magnetospheric compression effect (Huang & Cheng, 1991). However, due to the scarcity of TEC observations in such early years, the fine-scale ionospheric structures in a broad region could not be well revealed and the underlying mechanisms could not be further explored.

Facilitating from the wider and denser distribution of Global Navigation Satellite System (GNSS) observations in recent years, it was revealed that the TEC wavelike oscillating structures could occur simultaneously around the globe during geomagnetic storms that were suggested to be under the substantial control of penetration electric fields (PEFs) (e.g., Zhang et al., 2023). However, the mixed spatio-temporal variation of the non-geostationary GNSS observations and the employed de-trending method to large data may smooth out the contribution from some specific physical mechanisms. Recently, based on the TEC continuously observed along fixed receiver-satellite links by tracking the signals of Beidou Geostationary (BD-GEO) satellites, it was found that the storm-time ionospheric oscillation synchronized over wide longitudes could possibly be caused by the combining effect of PEFs and the refilling process due to plasma pressure difference (Li et al., 2019). In addition, the storm-time auroral energy input may trigger traveling ionospheric disturbances (TIDs) which could also be manifested as fluctuations of plasma density and height (e.g., Borries et al., 2017; Ding et al., 2007; Figueiredo et al., 2017; Habarulema et al., 2018; Shiokawa et al., 2012; Zakharenkova et al., 2016).

The storm-time ionospheric variations due to different physical mechanisms could appear in similar patterns, that is, periodic ionospheric oscillation/fluctuation in TEC, plasma density and/or height, which could not be well told apart from each other (e.g., Ding et al., 2007; Huang & Cheng, 1991; Li et al., 2019; Zhang et al., 2023). Under geomagnetic quiet or weak disturbed conditions, recent studies have demonstrated the great advantages of BD-GEO TEC observed along specific latitudes/longitudes in tracing fine-scale ionospheric disturbances and differentiating their complex mechanisms (e.g., Hao et al., 2024; Huang et al., 2017; Li et al., 2019; Sun et al., 2022; Xiong et al., 2023). It is still not clear that during very strong geomagnetic storms, how the ionosphere will behave in terms of fine-scale structures, that is, the ionospheric variations with short period within small regions that may exhibit significant gradient or fast change over very nearby locations. It is also important to figure out what the intrinsic differences between the fine-scale structures due to different mechanisms are, and which mechanism could dominate their generation and evolution over specific regions.

In May 2024, one of the strongest geomagnetic storms during the past 20 years occurred. This provides a good opportunity to address the questions raised above. During the storm, significant ionospheric fluctuations were observed over a large region in East and Southeast Asia. In this study, based on the BD-GEO TEC continuously observed along specific latitudes and longitudes, in combination with multiple other kinds of observations, we try to figure out the spatio-temporal features of the complex fluctuations and identify the potential factors controlling their generation and evolution.

2. Event Description, Data and Methods

The May 2024 super geomagnetic storm is the consequence of multiple consecutive coronal mass ejections. It reached G5 level with a minimum SYM-H (Dst) index −518 nT (−412 nT). According to the minimum SYM-H and Dst index, which rank the first since 2004, the present event could be the strongest storm during the past 20 years. Details of the storm evolution process could be seen in the recent papers (Guo et al., 2024; Spogli et al., 2024). Figure 1 presents the solar wind speed measured by the ACE satellite that was post-processed and archived in the OMNI database (https://spdf.gsfc.nasa.gov/pub/data/omni/high_res_omni/), Dst/SYM-H (https://wdc.kugi.kyoto-u.ac.jp/) and Kp (https://kp.gfz-potsdam.de/en/) indices during 09–13 May 2024. According to the SYM-H variation, the storm sudden commencement (SSC) was at ∼17:10 universal time (UT, Beijing local time LT = UT+8 hr) on 10 May, following an abrupt increase of solar wind speed from ∼450 km/s to ∼700 km/s. Note that it was post-midnight period for the East and Southeast Asian sector when the storm commenced. After that, the solar wind speed increased steppedly and reached the maxima ∼1,000 km/s at ∼01:00 UT on 12 May. The main phase of the storm lasted until ∼02:14 UT on 11 May when the SYM-H reached its minimum. During the process, the maximum Kp index reached 9. It is relevant to mention that the significant

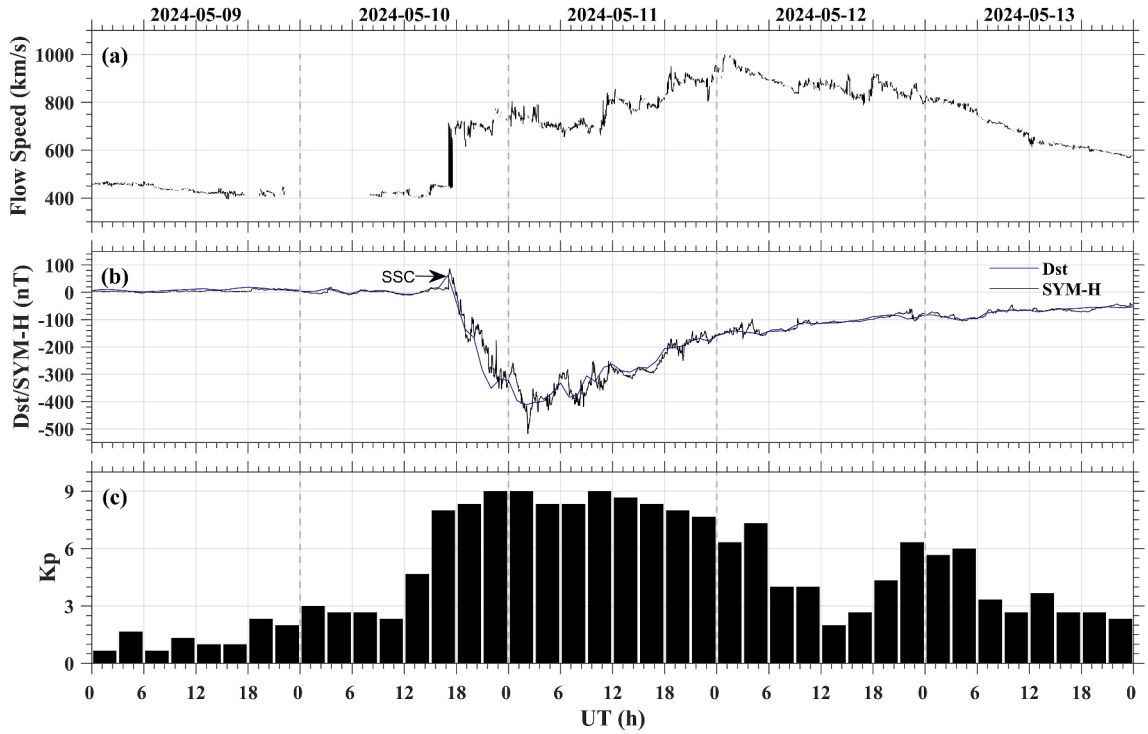

Figure 1. (a) The solar wind speed, (b) Dst/SYM-H and (c) Kp index during 09–13 May 2024. The black arrow in (b) indicates the storm sudden commencement (SSC).

increase of Kp (at ∼15:00 UT on 10 May) was a little earlier than the SSC seen from SYM-H. For this discrepancy, there could be two possibilities. (a) The Kp index is calculated based on the K index measured by ∼13 observatories at subauroral regions (Matzka et al., 2021), whereas the SYM-H is mainly obtained based on the relative variation of the geomagnetic field horizontal component H observed at middle and low latitudes (Wanliss & Showalter, 2006). The advanced enhancement of Kp index earlier than that of SYM-H may be partly due to the latitude discrepancy of instrument measurements that involved to generate the corresponding indices. (b) The temporal resolution of SYM-H is 1 min, whereas the temporal variation of Kp is 3 hr that may not well represent the fast variation of storm-time geomagnetic field.

In order to investigate the ionospheric behavior during the geomagnetic storm, three types of instruments are employed, including (a) GNSS receiver networks, (b) multiple ionosondes, and (c) a Low lAtitude long Range Ionospheric raDar (LARID) (Hu et al., 2024). Some of these instruments belong to the Chinese Meridian Project Phase I (Wang, 2010) and Phase II (Wang et al., 2023), and the International Meridian Circle Program (Liu et al., 2021). The distribution of the instruments is shown in Figure 2.

From the GNSS observations, the TEC could be calculated based on the same method as in previous studies and will not be repeated here (e.g., Liu et al., 2017; Sun et al., 2022; Xiong et al., 2016). The TEC fine-scale structures during the storm are mainly obtained via tracking the signals of BD-GEO satellites, which could provide continuous observations at fixed ionospheric pierce points (IPPs). The BD-GEO GNSS receivers are from the Ionospheric Observational Network for Irregularity and Scintillation in East/Southeast Asia (IONISE) (Li et al., 2019; Sun et al., 2020). As shown by blue dots in Figure 2, the TEC fine-scale structures could be traced along the fixed IPP arrays of 37°N, 21°N, 9°N and 110°E, respectively. Due to the different receiver distributions along the three latitudes, the number of BD-GEO satellite IPPs may also be different. Notably, the IONISE GNSS receivers could also track the signals of the Global Positioning System (GPS), the GNSS of Russia (GLONASS), and the European Galileo system. In combination with the Crustal Movement Observation Network of China (CMONOC; Aa et al., 2015), and other GNSS networks around the world including the International GNSS Service (IGS) Working Group on ionosphere (Beutler et al., 1999) and the Geoscience Australia network (https://www.ga.gov.au), the TEC behavior over a large region could be obtained. The sampling rate of TEC is 30 s. The IPPs are projected at the F-region altitude 300 km. To indicate the increase and decrease of TEC with time, the

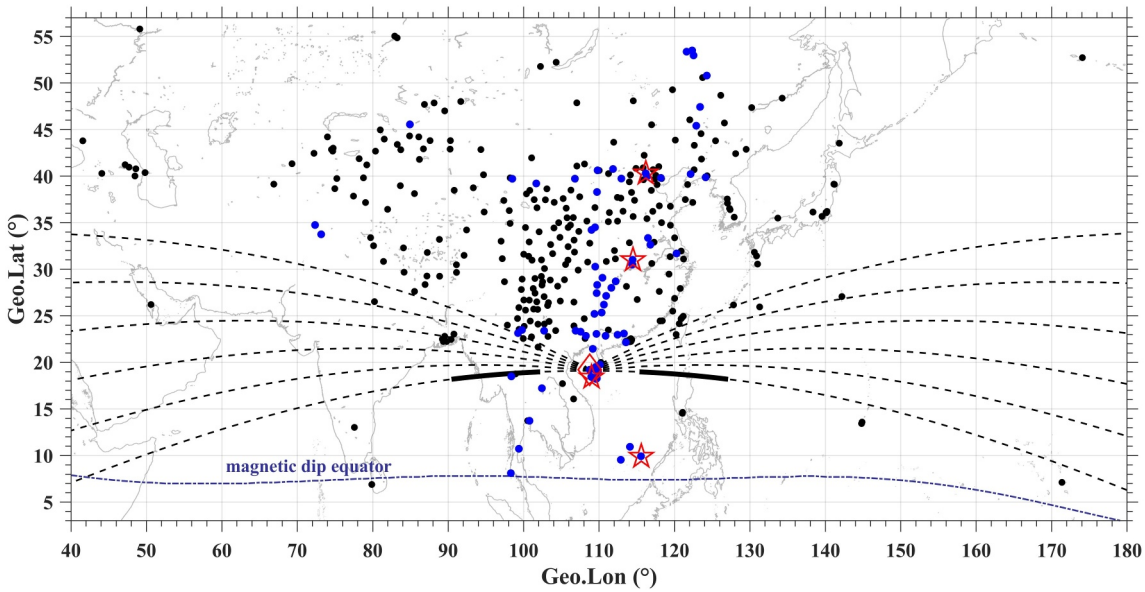

Figure 2. The distribution of the observational instruments employed in the present study. The red stars, red diamond, blue and black bold dots represent ionosndes, the Low lAtitude long Range Ionospheric raDar (LARID), GNSS receivers from IONISE and from other observational networks, respectively. The blue dotted curve denotes the magnetic dip equator. The black dashed curves denote the LARID beam directions. The black bold curves superimposed on the beam directions mark the approximate locations of the ionospheric reflection points for the ground scatters detected by the range gates 1,500–4,000 km.

rate of TEC change (ROT) is employed. Note that the ROT is different from the rate of TEC index (ROTI) usually used to characterize the occurrence of ionospheric irregularities.

In order to investigate the occurrence of TIDs during the storm, the de-trended TEC (dTEC) is used. For the dTEC calculation, proper detrending to accurately identify the desired features of wavelike structures is important (Guerra et al., 2024). For the present study, dTEC was calculated by subtracting the 1-hr running average of the vertical TEC data. Then the dTEC was projected at 300 km altitude and binned into $1° \times 1°$ grids every 5 min. The average of all the data within each grid area was chosen to represent the value of the grid. For TEC, ROT and dTEC, only the data with elevation angles higher than 30° was used.

To investigate the ionospheric variations at typical latitudes, ionogram observations by the ionosondes distributed along ∼110–120°E, including Meiji (115.6°E, 9.9°N, magnetic latitude 2.8°), Ledong (109.0°E, 18.4°N, magnetic latitude 12.9°), Wuhan (114.5°E, 31.0°N, magnetic latitude 28.0°) and Beijing (116.2°E, 40.3°N, magnetic latitude 39.4°), are employed. The ionograms, with sampling rates of 5, 7.5, 15 and 15 min, respectively, were manually scaled for obtaining the plasma density profiles below the F layer peak. Note that the largest detection range for the Meiji, Ledong, Wuhan and Beijing ionosondes are 1,200, 1,280, 1,280 and 650 km, respectively.

The LARID is an over-the-horizon high frequency radar newly built at the low-latitude station Dongfang (19.2°N, 108.8°E, magnetic latitude 13.9°) in 2023. Details of LARID could be seen in Hu et al. (2024). The LARID consists of two subsystems which can be operated looking toward east and west respectively. For either direction, the subsystem includes a main transmitting/receiving array consisting of 20 log-periodic antennas and a receiving interferometry array consisting of 4 similar antennas. Whereas one main purpose of LARID is to observe equatorial plasma bubbles by receiving irregularity backscatter echoes, here we use the ground scatters by LARID to derive the background ionospheric variability (Sun, Li, Nang, et al., 2024). During the present experiment, the LARID was operated at 20.4 MHz with a beam steering mode stepped by 5°. The beams were within the azimuth 65°–90° for the east beams and −90° to −65° for the west beams (clockwise due north). Based on the simulation by Hu et al. (2024), the beams center at ∼17°, with a 3-dB beam width of ∼18° in the elevation direction. The number of range gates is 160 with a range resolution of 60 km, attaining a maximum range of ∼9600 km at each side. By employing a virtual height model (Chisham et al., 2008), the group range of LARID observations could be mapped to geographic longitudes (Figure 2).

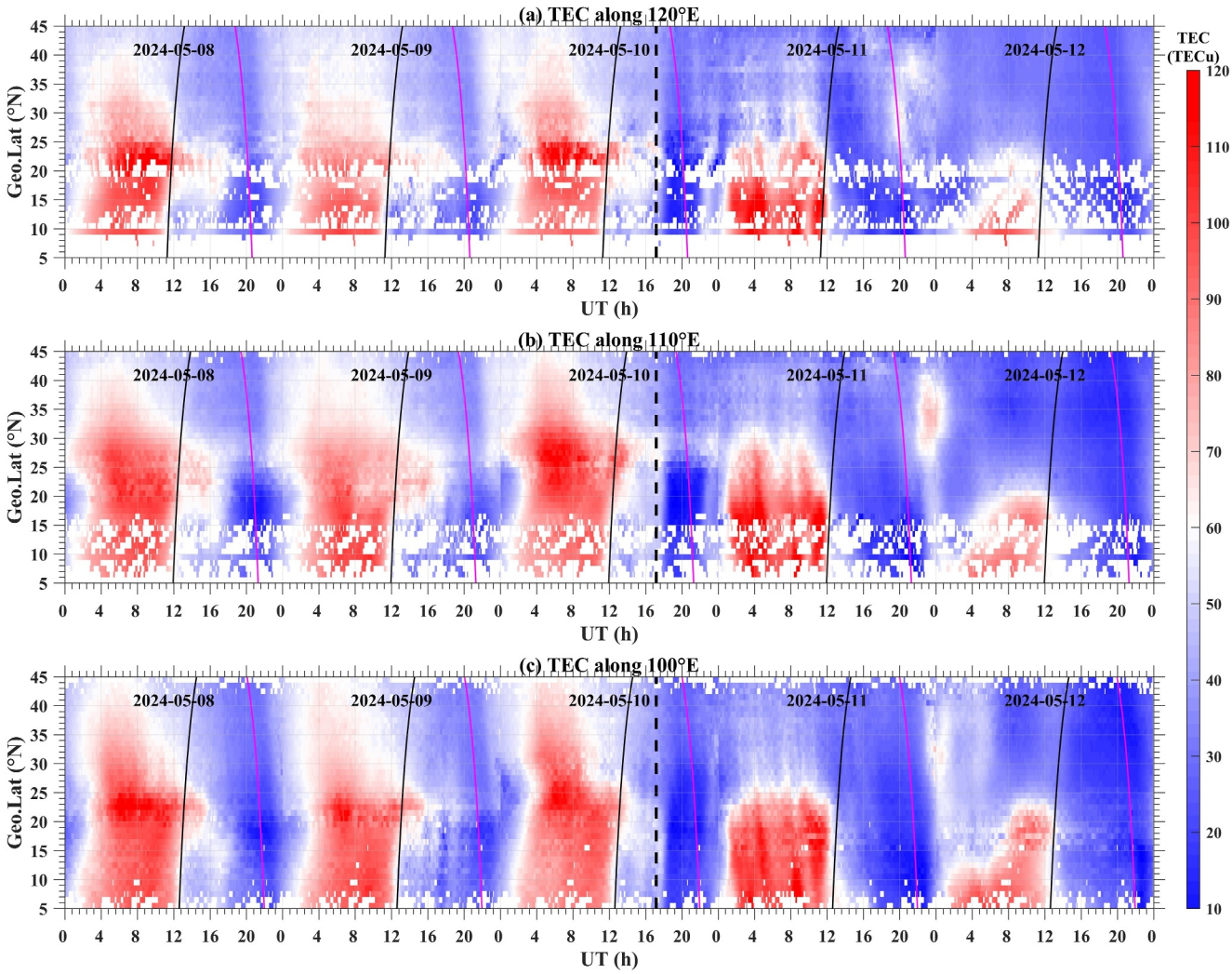

Figure 3. The TEC keograms along (a) 120°E, (b) 110°E and (c) 100°E during 08–12 May 2024. The magenta and black solid curves in each panel denote the sunrise and sunset terminators at 300 km altitude over different latitudes along the corresponding longitude of each panel, respectively. The black dashed lines mark the storm sudden commencement.

3. Results

In order to get an overview of the ionospheric response to the storm over East and Southeast Asia, Figure 3 shows the TEC keograms along three selected longitudes 120°E, 110°E and 100°E, respectively. From Figure 3, the equatorial ionization anomaly (EIA) on May 11 and 12 was not fully developed, as compared with that on quiet days. This was possibly due to a suppressed fountain effect. Note that the suppression was more significant on 12 May than on 11 May. The suppressed EIA consequently caused the negative ionospheric storm at middle to low latitudes. One interesting feature noted from Figure 3 is that there seem to be multiple stripes elongating from middle to low or even equatorial latitudes in the TEC keograms on 11 May. This is quite different from the patterns on the other days, indicating that the TEC at a specific latitude may vary periodically over time. Further, comparing the observations shown in different panels of Figure 3, we can find that the TEC variation exhibited similar but not completely the same behavior over different longitudes. For example, the EIA suppression and stripes elongating from middle to low latitudes could be observed over all the three adjacent longitudes, but the suppressed EIA morphology was not exactly the same. The observations indicate that fine-scale structures may exist during the event. In the present study, we will mainly focus on the periodic variations rather than the positive/negative storm effects or the EIA shift during storms which have been well investigated in previous studies.

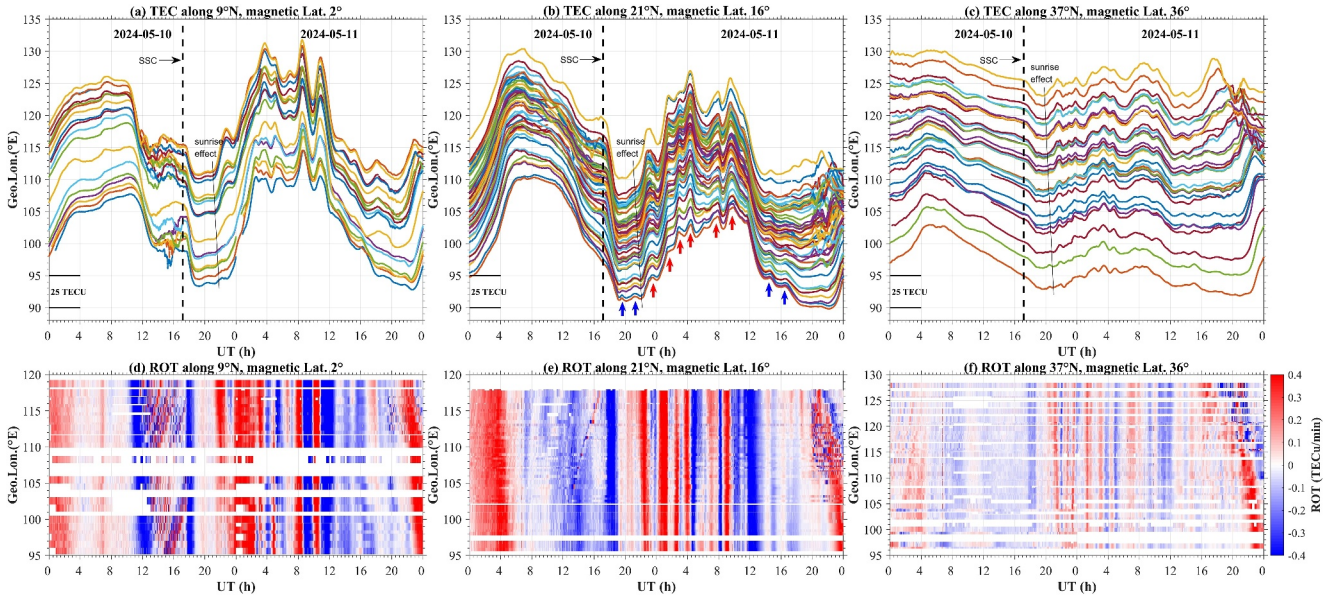

Figure 4. The TEC observed at the fixed IPPs along (a) 9°N (b) 21°N and (c) 37°N, and (d)–(f) the corresponding rate of TEC change (ROT). The black dashed lines mark the storm sudden commencement. The black solid lines mark the TEC increase due to sunrise. The blue and red arrows in the panel b mark the TEC fluctuation crests during nighttime and daytime, respectively.

Figures 4a–4c present the BD-GEO TEC continuously observed at the fixed IPPs along three latitudes, the equatorial latitude 9°N (magnetic latitude ∼2°N), the low latitude 21°N (magnetic latitude ∼16°N) and the middle latitude 37°N (magnetic latitude ∼36°N). Figures 4d–4f present the corresponding ROT. Compared with the observations before the storm, the TEC variation after the SSC showed obvious fluctuations with multiple crests embedded in the diurnal variation, which was the most remarkable over low latitude (i.e., 21°N), with up to 10 fluctuation crests as indicated by the upward arrows in Figure 4b. The TEC fluctuation was more significant during the daytime (indicated by red arrows), and could also be observed during nighttime but with smaller amplitudes (indicated by blue arrows). For the fluctuation amplitudes at different latitudes, they were larger at equatorial and low latitudes (up to more than 10 TECu, Figures 4a and 4b) than at middle latitudes (predominantly smaller than 3 TECu, Figure 4c). Further, based on the corresponding ROT observations (Figures 4d–4f), the TEC increases (indicated by positive ROT) and decreases (indicated by negative ROT) for the fluctuations along the same latitude were nearly synchronized in a large longitude span up to 35°. It is relevant to mention that before the SSC, ionospheric disturbances could also be observed, especially at the equatorial latitude during 12:00-16:00 UT on 10 May. These disturbances showed depletion morphology and were due to the general occurrence of EPBs, which have been investigated in our companion paper (Sun, Li, Zhao, et al., 2024) and will not be further focused on in the present study.

Figure 5 presents the ionospheric density profiles below the F layer peak observed by the ionosondes at different latitudes. Note that for the Beijing observation, there was a long duration of data gap from ∼22:00 UT on 10 May to ∼08:30 UT on 11 May. For the data gap, one possibility is the significant uplift of the mid-latitude ionosphere similar to that reported by Spogli et al. (2024), which led to a very high F layer exceeding the largest detection range of the Beijing ionosonde 650 km. However, the uplift process was not well observed by the Beijing ionosonde due to the abrupt absence of trace echoes since ∼22:00 UT on 10 May. Nevertheless, from Figure 5, we can find that different from the patterns before the storm (e.g., before SSC on 10 May), the profiles after the SSC showed significant fluctuations in both the plasma frequency and height, especially on 11 May. The plasma density and height fluctuations could consequently contribute to the fluctuations of TEC. The profile fluctuations during the daytime of 11 May were more significant over the magnetic equator (i.e., Meiji) and low latitude (i.e., Ledong), corresponding well with the TEC fluctuations at different latitudes. The fluctuations after sunset were likely originated from higher latitudes and extended all the way from middle latitudes to the magnetic equator, as marked by the black arrows, indicating a possible equatorward propagation.

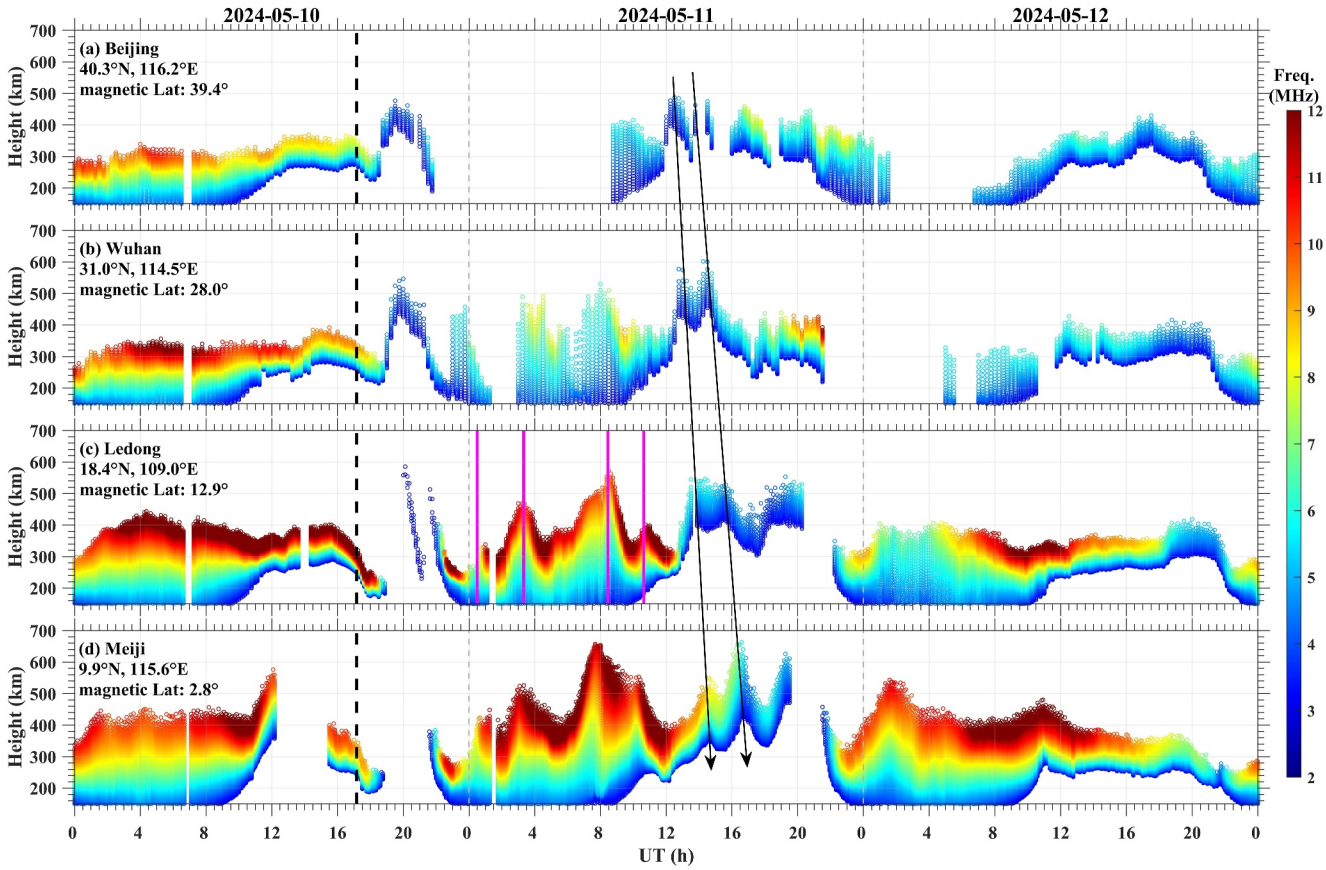

Figure 5. The ionospheric density profiles obtained by the ionosondes at different latitudes. The black dashed line in each panel indicates the storm sudden commencement. The magenta lines in (c) mark the specific time intervals 00:30, 03:20, 08:27, and 10:38 UT on 11 May when the Ledong ionospheric profile showed fluctuation crests.

In order to investigate the latitudinal variation of the TEC fluctuations, the ROT calculated from BD-GEO TEC observations at fixed IPPs along 110°E ± 10° during 10–12 May are presented in Figure 6, along with the simultaneous auroral electrojet (AE) index, interplanetary magnetic field (IMF) Bz and the ionospheric density profile observed at the magnetic equatorial site Meiji. As can be seen, the TEC fluctuations characterized by positive or negative ROT after the SSC could either be originated from the equatorial region and extend poleward, or be originated from higher latitudes and propagate equatorward. The poleward extending fluctuations were mainly constrained at equatorial and low latitudes (e.g., below 20°N magnetic latitude). The equatorward propagating fluctuations could reach the magnetic equator, for example, the fluctuations indicated by the blue arrows labeled as "6" and "7".

4. Discussion

Previous studies on the TEC behaviors during strong geomagnetic storms mainly focused on the positive or negative storm effects on global or hemispheric scales during different phases of storm development (e.g., Balan et al., 2010; Fejer, 2002; Kuai et al., 2016; Lu et al., 2008; Nava et al., 2016; Prölss & Werner, 2002; Zhang et al., 2017; Zhao et al., 2012). For the May 2024 super geomagnetic storm, one interesting feature of the TEC behavior over East and Southeast Asia is the synchronized TEC fluctuations in a wide longitude range, with up to 10 oscillating crests embedded in the diurnal variation.

Similar TEC pattern was occasionally observed previously at single station during super geomagnetic storm event. For example, Huang and Cheng (1991) reported wavelike TEC oscillation near the EIA region during the March 1989 super geomagnetic storm (minimum Dst −589 nT), which was attributed to the compression/expansion of the plasmasphere pushing the ionization into/out of the ionosphere. In their studies, the TEC was

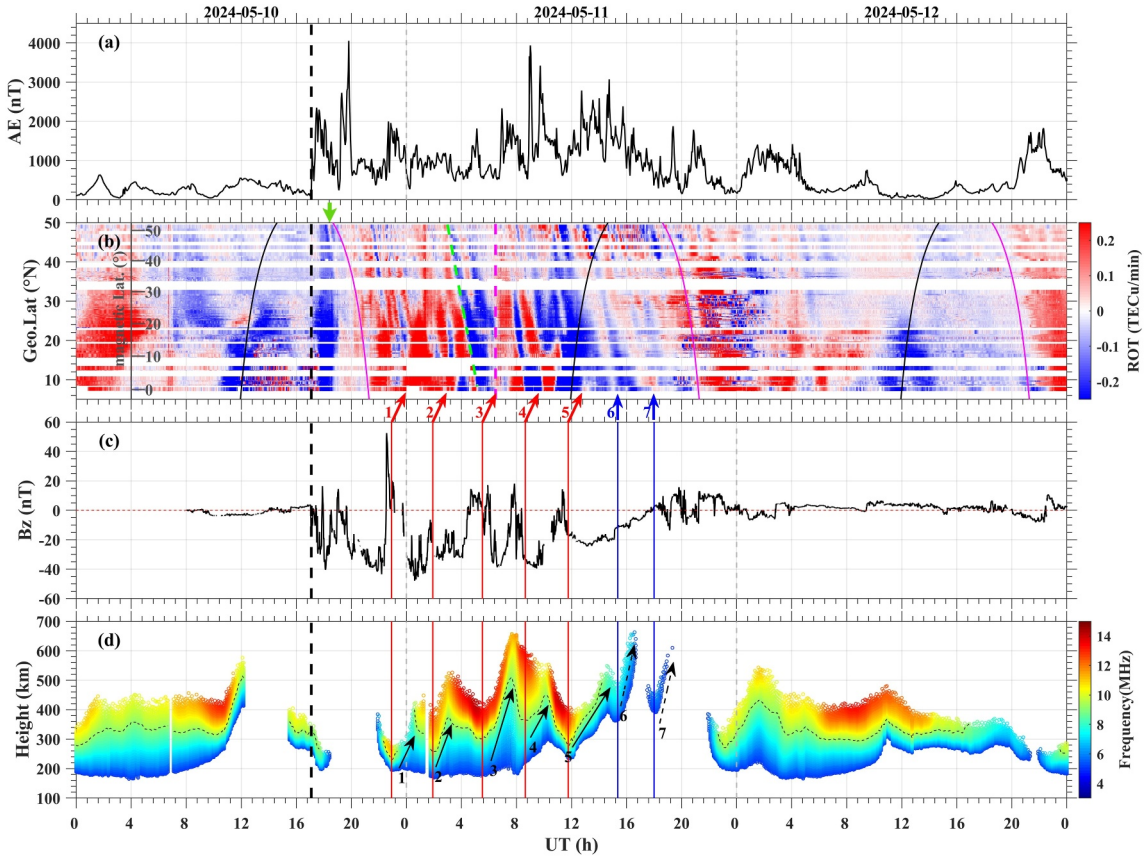

Figure 6. The (a) AE index, (b) ROT as functions of UT and latitude over 100–120°E, (c) IMF Bz, and (d) the bottomside ionospheric profile obtained by the ionosonde at Meiji. The black dashed line in each panel indicates the storm sudden commencement. In (b), the magenta and black curves denote the sunrise and sunset time at the F region height 300 km over different latitudes along 110°E, the green slant dashed line marks the propagation of one well distinguished wavefront of equatorward disturbance, and the magenta vertical dashed line marks the enhanced positive ROT nearly simultaneously from equatorial to middle latitudes. In (c), the red dashed line marks the value of zero. In (d), the black dashed curve marks the height variation with plasma frequency 9 MHz. The black solid and dashed slant arrows indicate the upward plasma drifts. The red and blue solid lines mark the starting time of upward plasma drifts. The red arrows between (b) and (c) indicate the TEC increase after the upward plasma drift. The blue arrows indicate two wave fronts extending from middle latitudes to equatorial latitudes. The green downward arrow between (a) and (b) indicates the time when equatorward propagating TID was initially observed.

measured by tracking the satellites at 2,000 km height, which is far below the magnetopause at the distance 4–10 times of the earth radius away from the ground. However, the TEC measured by tracking BD-GEO satellites in the present study could be up to 36,000 km. The plasma above this height may contribute very small (in the order of 10^{-1} TECu) to the integrated TEC (e.g., Hao et al., 2017). Therefore, the compression/expansion of the plasmasphere may not be the major driving mechanism for the TEC fluctuations with amplitudes up to ∼10 TECu observed in the present study.

Regarding TEC oscillations synchronized over a wide longitude span, Li et al. (2019) reported a case during a moderate geomagnetic storm with minimum Dst index −86 nT, which was associated with periodic changes in IMF Bz polarity. However, the TEC oscillations observed by Li et al. (2019) were mainly constrained at low latitudes during nighttime, with small oscillating amplitudes below 0.5 TECu. In the present study, remarkable TEC fluctuations could be observed from equatorial to middle latitudes during both daytime and nighttime, with much larger fluctuating amplitudes up to 10 TECu. Nevertheless, the observations by Li et al. (2019) suggest that multiple penetrations of interplanetary electric fields indicated by IMF Bz oscillation could contribute to the TEC oscillation synchronized over wide longitudes. Recently, Zhang et al. (2023) reported simultaneous global ionospheric disturbances derived from the worldwide TEC data that were suggested to be under the substantial control of storm-time PEFs.

For the present study, the poleward extending component of the TEC fluctuations originated from the magnetic equator could be linked with PEFs. The possible presence of PEFs could be indicated by the variations of IMF Bz

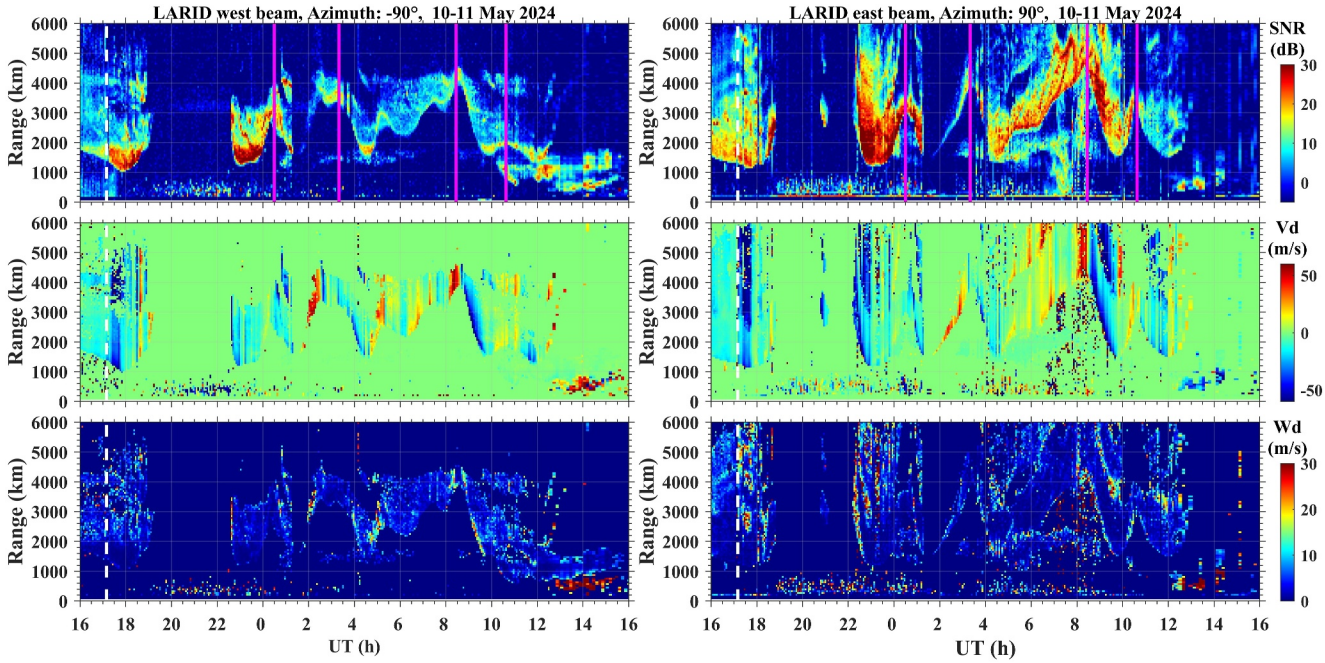

Figure 7. The SNR, Doppler velocity and spectral width of the echoes by LARID beams on 10–11 May 2024. The white dashed line in each panel indicates the storm sudden commencement. The magenta lines mark the specific time intervals 00:30, 03:20, 08:27, and 10:38 UT on 11 May when the echoes showed as fluctuation crests.

and the ionospheric plasma density profiles observed at the equatorial site Meiji. During the period of these fluctuations, the polarity of IMF Bz (Figure 6c) and the bottomside ionospheric profile over the magnetic equator (Figure 6d) also oscillated apparently. The black solid arrows in Figure 6d mark several periods when the oscillation phase of the ionospheric profile over the magnetic equator was upward. These upward plasma drifts were predominantly associated with southward IMF Bz. Generally, eastward PEF could be established following the southward excursion of IMF Bz or significant jump in IMF Bz toward more southward at the dayside or even before pre-midnight in the ionosphere via the undershielding process (e.g., Huang et al., 2007; Spogli et al., 2021; Wei et al., 2015; Zhang et al., 2023), which then leads to upward plasma drift through $\mathbf{E} \times \mathbf{B}$. Corresponding with each onset of the upward plasma drifts (marked by red solid lines in Figures 6c and 6d), the TEC over the equatorial region may decrease at first, and increase about 1 hr later, as marked by the red arrows labeled "3" and "4" in Figure 6. This is because the upward plasma drift would transport plasma to higher latitudes (e.g., low latitudes) through the fountain effect, which will cause the initial plasma loss over the magnetic equator. Then due to the reduced recombination rate at higher altitudes and/or the replenishment from photochemical production, the TEC over the magnetic equator will increase again. The initial TEC decrease due to transport loss may not be obvious before noon when the fast photochemical production could compensate the transport loss quickly (e.g., as indicated by the red arrow labeled "1" and "2" in Figure 6), whereas after sunset the TEC increase subsequent to the initial transport loss may not be obvious due to the absence of photochemical production (e.g., as indicated by the red arrow labeled "5" in Figure 6).

In order to further verify the presence of PEFs over a large longitude span, Figure 7 presents the echoes observed by the LARID west and east beams, which showed remarkable fluctuations after the storm commenced. The magenta lines in the top panels of Figure 7 mark four specific time intervals 00:30, 03:20, 08:27, and 10:38 UT on 11 May, when the echoes of the beams in the two directions simultaneously showed fluctuation crests. The Doppler velocity before (after) the crests were mainly positive (negative), indicating the echoing region moving away from (toward) the radar. Whereas the Doppler velocities of the fluctuating echoes were remarkably large (beyond ±60 m/s), the spectral widths were predominantly narrow (<10 m/s), indicating that the echoes could be 1-hop ground scatters reflected by the ionosphere rather than irregularity backscatter echoes. The fluctuations of these ground scatters corresponded well with the ionospheric profile oscillations observed by the Ledong ionosonde (Figure 5c), where oscillation crests also occurred around the time intervals 00:30, 03:20, 08:27, and 10:38 UT (marked by the magenta lines in Figure 5c). Since the LARID beams and the Ledong ionosonde are nearly in the same low latitude

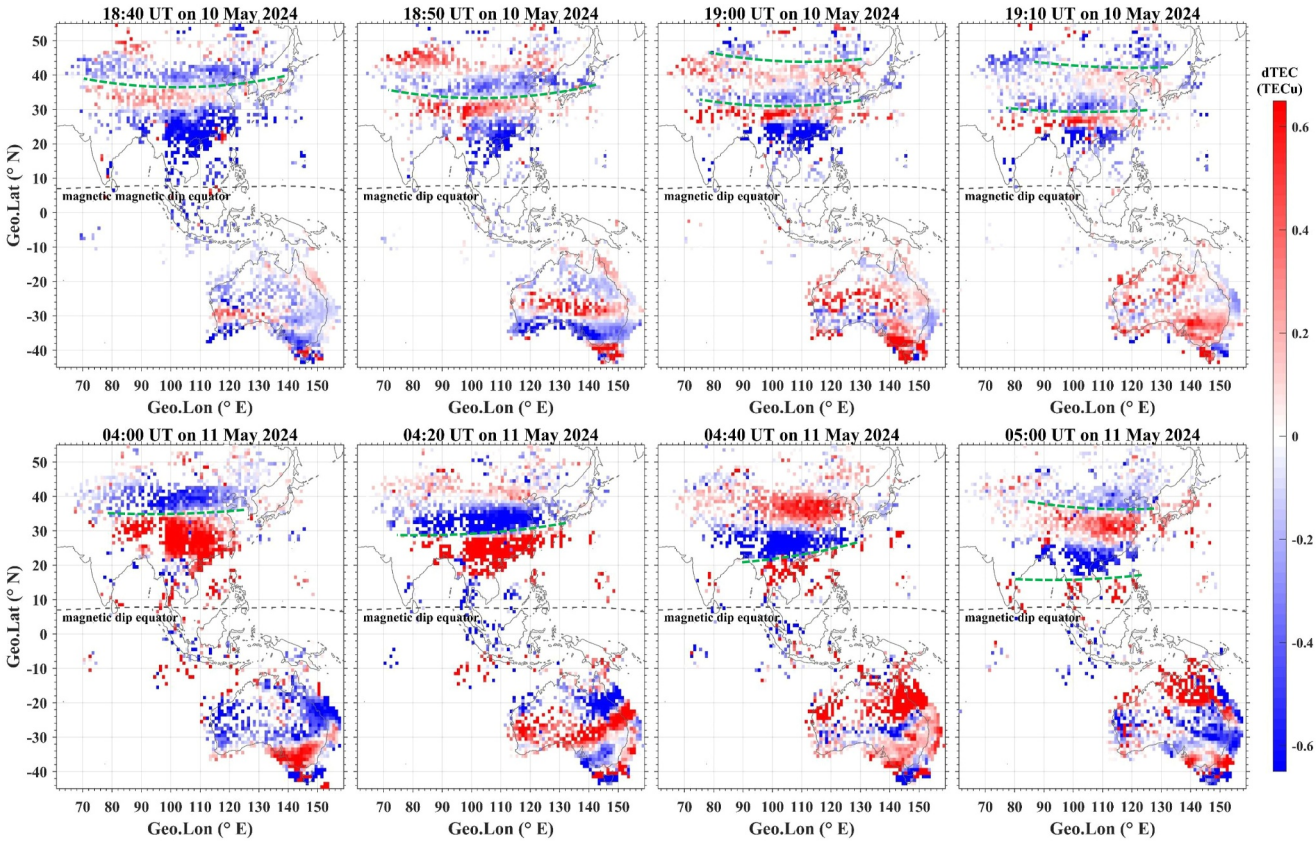

Figure 8. Two sequences of de-trended TEC (dTEC) maps during 18:40–19:10 UT on 10 May and 04:00–05:00 UT on 11 May, respectively. The gray dashed curve in each panel denotes the magnetic dip equator. The green dashed curves roughly denote the distinguished wave fronts.

(i.e., 18.4°N, magnetic latitude 12.9°), the fluctuations could be due to the same mechanism, that is, the PEFs. The rapid vertical drifts caused by PEFs could lead to fast displacement of suitable ionospheric reflection points for ground scatters along the ray paths, which then were manifested as significant range variation and large Doppler velocities. For the ionospheric reflection points for ground scatters, their distances from the LARID could be roughly estimated as $\frac{R}{2} \times \cos(\theta)$, where R and θ denote the echo range and beam elevation angle respectively (Sun, Li, Nang, et al., 2024). Considering the majority of echo ranges ∼1,500–4,000 km and assuming the beam elevation angle 17°, the LARID observations could partly indicate the presence of PEFs at the distance ∼700–1,900 km away from the radar in the east and west directions respectively (as marked by the black bold curves in Figure 2). It is relevant to mention that since the true elevation angle of the radio waves are unknown at present, the accurate positions of the ionospheric reflection points could not be well obtained. Nevertheless, the observations by LARID indicate that the PEF could be present in a large zonal span up to ∼3,800 km.

In addition to the TEC fluctuations originated from the magnetic equator and extending poleward, there was another kind of fluctuation sourced from higher latitudes and propagating equatorward (Figure 6b). These TEC fluctuations were most likely linked with TIDs originated from high latitude and polar regions. Figure 8 presents two sequences of dTEC maps during 18:40–19:10 UT on 10 May and 04:00–05:00 UT on 11 May to represent the TID occurrences during nighttime and daytime respectively. Three features could be seen. (a) The dTEC maps showed the signatures of TIDs in both hemispheres. The TID wave fronts over China (marked by the green dashed curves in Figure 8) mainly elongated in the east-west direction, corresponding well with the synchronized TEC oscillation in a large longitude span along the same latitudes (Figure 4). (b) Based on the distances between adjacent wave fronts, the wavelengths of the TIDs could be roughly estimated. For the TID during 18:40–19:10 UT on 10 May (04:00–05:00 UT on 11 May), the distance between adjacent wave fronts spanned ∼13° (20°) in latitudes, for example, at 19:00 UT (05:00 UT), corresponding to the wavelength of ∼1,300 km (2,000 km). (c) The TIDs in both hemispheres propagated equatorward. Based on the displacement of the same wavefront over

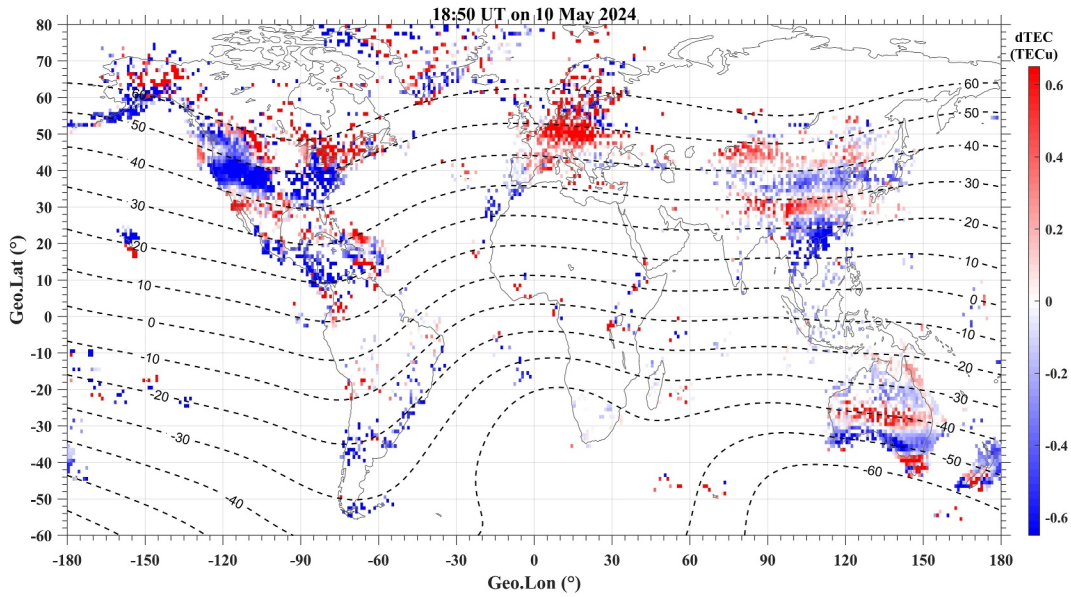

Figure 9. The dTEC map at 18:50 UT on 10 May 2024. The dashed contours denote different magnetic dip latitudes.

time in different dTEC maps, the propagating velocity of the TIDs could be estimated (Ding et al., 2014). For the TID during 18:40–19:10 UT on 10 May (04:00–05:00 UT on 11 May), the same wavefront migrated ∼7° (19°) in latitudes during 0.5 hr (1 hr), corresponding to ∼700 km (1,900 km). Therefore, the average propagating velocity of the TID during 18:40–19:10 UT on 10 May (04:00–05:00 UT on 11 May) was estimated to be ∼389 m/s (528 m/s).

To further verify the calculation result, we also estimated the TID propagating velocity based on the ROT keogram in Figure 6b. In the ROT keogram, the TID propagating from polar regions to lower latitudes were manifested as multiple positive/negative ROT stripes. The TID propagating velocity could be roughly estimated based on the slopes of the stripes. The stripe around 04:00–05:00 UT on 11 May could be well distinguished and is marked by a green slant dashed line. Based on the slope of the green dashed line, the TID average propagating velocity around 04:00–05:00 UT was ∼520 m/s, corresponding well with the result obtained based on the dTEC maps. Similar TID propagating velocity was also reported in previous studies. For the October 2003 super magnetic storm (minimum Dst −383 nT, maximum AE 4,500 nT), the TID propagating velocity was estimated to vary within 270–738 m/s over China region (Ding et al., 2007), which is in the same order with our observations during the May 2024 super storm. According to the wavelengths and propagating velocities, these TIDs could be categorized as large-scale TIDs (LSTIDs) (e.g., Borries et al., 2017; Ding et al., 2007).

During geomagnetic storms, LSTIDs were usually observed propagating equatorward, which were suggested to be triggered by the auroral energy input linked with Joule heating (e.g., Borries et al., 2016; Ding et al., 2007; Figueiredo et al., 2017; Shiokawa et al., 2012). As can be seen from Figure 6, the earliest equatorward TID signature after the SSC was observed around ∼18:30 UT at ∼50°N (as marked by the green arrow in Figure 6), which was delayed by about 80 min after the abrupt AE increase at ∼17:10 UT. The delay time is consistent with the general response time for mid-latitude ionosphere to auroral energy input (e.g., Prölss, 1993). From ∼18:30 UT on 10 May to ∼08:00 UT on 12 May, obvious TID signatures could be continuously observed at middle latitudes associated with active auroral energy input (indicated by AE larger than 1000 nT). After that, as AE gradually weakened, obvious TID signature also diminished. It is relevant to mention that if the LSTID is triggered by auroral energy input, it may occur at all meridians around the globe. As shown in Figure 9, the LSTIDs were clearly observed in Asian and American sectors during the present storm. The occurrences of LSTIDs over different longitude sectors further indicate that they could be sourced from the auroral energy input.

Regarding the latitude range of TEC fluctuations under different mechanisms, the fluctuations driven by PEFs were mainly constrained at equatorial and low latitudes, whereas those linked with TIDs generally existed at middle or higher latitudes. However, there were also some exceptions. For example, the TIDs occurring during

12:00–18:00 UT on 11 May were observed propagating from middle (~50°N) to equatorial latitude (~7°N), as indicated by the blue arrows labeled "6" and "7" in Figure 6. Correspondingly, the fluctuations observed in the ionospheric profiles (Figure 5) also migrated from middle (i.e., Beijing) to equatorial latitude (i.e., Meiji), as marked by the black arrows. Therefore, for the upward plasma drift observed at Meiji during ~12:00–15:00 UT (indicated by the black arrow labeled "5" in Figure 6d), it could be the combining effects from PEF and TID propagation. However, for the profile oscillations afterward (indicated by the black dashed arrows labeled "6" and "7" in Figure 6d), they were more likely to be dominated by TID propagation, due to the fact that it was post-midnight when the condition is usually unfavorable for inducing eastward PEF to drive upward plasma drift (e.g., Wei et al., 2015). On the other hand, whereas the PEF inducing TEC fluctuations were mainly constrained at equatorial and low latitudes, they may also influence higher latitudes. For example, the fluctuation occurring at ~06:00 UT on 11 May (as marked by the magenta vertical dashed line in Figure 6b) was manifested as enhanced TEC increasing rates (enhanced positive ROT) nearly simultaneously from equatorial to middle latitudes. These fluctuations simultaneously observed over a large latitude span were similar to the disturbances illustrated by Zhang et al. (2023), which were suggested to be associated with the PEF effect. Therefore, comparing with middle and equatorial latitudes, the low-latitude region is more likely to be affected by the disturbances originated from both the auroral energy input and the equatorial electrodynamics and thus exhibit the most complex feature. That is why the ionospheric fluctuations shown in Figure 4 were more remarkable over low latitude (panel b) than other latitudes (panels a and c).

It is relevant to mention that besides the Asian sector, wavelike fluctuations were also observed by Spogli et al. (2024) in the European sector during the present storm, which were also suggested to be the joint action of equatorial/low-latitude electrodynamics and wavelike perturbations sourced from high latitude and polar regions. However, comparing with the observations in the European sector by Spogli et al. (2024), the complex ionospheric fluctuations in the Asian sector shown by the present study seem more significant, with more TEC oscillation crests and larger fluctuation magnitudes. There could be two possibilities. (a) The observations by Spogli et al. (2024) were mainly performed at the middle latitudes higher than 35°N, whereas the most significant ionospheric oscillations in the present study were observe at low latitudes. It is more difficult for the disturbances originated from equatorial regions to reach middle latitudes. (b) The local time of the European sector lags ~6 hr behind the East Asian sector. For the period with most active IMF Bz variation (from ~16:00 UT on10 May to 12:00 UT on 11 May), the Asian sector was mainly in the daytime whereas the European sector was mainly in the nighttime. For the daytime (nighttime) sector, it is generally more (less) favorable for the IMF Bz fast variation to induce eastward PEF which then could trigger disturbances originated from the magnetic equator (e.g., Wei et al., 2015).

5. Summary

In this study, complex ionospheric fluctuations over East and Southeast Asia were observed during the May 2024 super geomagnetic storm. Based on multiple observations from equatorial to middle latitudes, the fine-scale structures of the complex fluctuations are investigated. The main results are concluded as follows.

1. The ionospheric fluctuations occurred following the storm commencement, and created multiple oscillating crests embedded in the TEC diurnal variation, with oscillating amplitude up to 10 TECu. Along the same latitude, the fluctuations were nearly synchronized over a wide longitude span up to 35°, which contained two major origins over the magnetic equator and high latitudes respectively.
2. The fluctuations originated from the magnetic equator could be due to multiple penetrations of the eastward electric field associated with southward excursion of IMF Bz. They generally extended poleward and were mainly limited at equatorial and low latitudes. The fluctuations originated from high latitudes were manifested as large-scale TIDs propagating equatorward probably around the globe, which could be triggered by storm-time auroral energy input. They generally existed at middle and higher latitudes but could also reach the magnetic equator.
3. Over different latitudes, the fluctuations at low latitude were the most significant and complex, which were under the influence by the disturbances sourced from both equatorial and high-latitude regions. Over different longitude sectors (e.g., the European and Asian sectors), the fine-scale ionospheric behavior may exhibit different features possibly depending on local time, which calls for further studies from a global perspective.

Data Availability Statement

The GNSS, ionosonde, LARID, and magnetometer data were obtained from the Geophysics Center, National Earth System Science Data Center at BNOSE, IGGCAS (http://wdc.geophys.ac.cn/dbList.asp), the Chinese Meridian Project (http://data.meridianproject.ac.cn), the Geoscience Australia GNSS data repository (https://data.gnss.ga.gov.au/docs/), and the UCSD GNSS database (ftp://garner.ucsd.edu/pub/rinex). The Kp index is provided by the GFZ Helmholtz Centre Potsdam (https://kp.gfz-potsdam.de/en/). The Dst and SYM-H are provided by the World Data Center for Geomagnetism, Kyoto (https://wdc.kugi.kyoto-u.ac.jp/). AE was reproduced from the online quick-look plots created on 6 June 2024 (https://wdc.kugi.kyoto-u.ac.jp/ae_realtime/). The solar wind speed and IMF Bz are obtained from the OMNI database (https://spdf.gsfc.nasa.gov/pub/data/omni/high_res_omni/). All the data used in this study are archived at the Beijing National Observatory of Space Environment, Institute of Geology and Geophysics, Chinese Academy of Sciences, and can be accessed at the WDC for Geophysics, Beijing (Sun, 2024).

Acknowledgments

This work was supported by the Project of Stable Support for Youth Team in Basic Research Field, CAS (YSBR-018), the National Natural Science Foundation of China (42404180), the Solar-Terrestrial Environment Research Network (STERN) of Chinese Academy of Sciences, the International Partnership Program of Chinese Academy of Sciences (Grant 183311KYSB20200003), and the Chinese Meridian Project. Work at MIT is supported by US NSF awards AGS-2033787, AGS-2149698, and AGS-1952737, and US NRL Grants N00014-23-1-2160 and N00014-24-1-2122. The authors acknowledge the Integrated Research Center for Islands and Reefs Sciences, Chinese Academy of Sciences (http://www.djzx.ac.cn/) for the maintenance of the instruments at Meiji.

References

Aa, E., Huang, W., Liu, S., Shi, L., Gong, J., Chen, Y., & Shen, H. (2015). A regional ionospheric TEC mapping technique over China and adjacent areas: GNSS data processing and DINEOF analysis. *Science China Information Sciences*, *58*(10), 1–11. https://doi.org/10.1007/s11432-015-5399-2

Abdu, M. A. (1997). Major phenomena of the equatorial ionosphere-thermosphere system under disturbed conditions. *Journal of Atmospheric and Solar-Terrestrial Physics*, *59*(13), 1505–1519. https://doi.org/10.1016/s1364-6826(96)00152-6

Balan, N., Shiokawa, K., Otsuka, Y., Kikuchi, T., Vijaya Lekshmi, D., Kawamura, S., et al. (2010). A physical mechanism of positive ionospheric storms at low latitudes and midlatitudes. *Journal of Geophysical Research*, *115*(A2), A02304. https://doi.org/10.1029/2009JA014515

Beutler, G., Rothacher, M., Schaer, S., Springer, T. A., Kouba, J., & Neilan, R. E. (1999). The International GPS Service (IGS): An interdisciplinary service in support of Earth sciences. *Advances in Space Research*, *23*(4), 631–653. https://doi.org/10.1016/S0273-1177(99)00160-X

Borries, C., Jakowski, N., Kauristie, K., Amm, O., Mielich, J., & Kouba, D. (2017). On the dynamics of large-scale traveling ionospheric disturbances over Europe on 20 November 2003. *Journal of Geophysical Research: Space Physics*, *122*(1), 1199–1211. https://doi.org/10.1002/2016JA023050

Borries, C., Mahrous, A. M., Ellahouny, N. M., & Badeke, R. (2016). Multiple ionospheric perturbations during the Saint Patrick's Day storm 2015 in the European-African sector. *Journal of Geophysical Research: Space Physics*, *121*(11), 11333–11345. https://doi.org/10.1002/2016JA023178

Chisham, G., Yeoman, T. K., & Sofko, G. J. (2008). Mapping ionospheric backscatter measured by the SuperDARN HF radars – Part 1: A new empirical virtual height model. *Annales Geophysicae*, *26*(4), 823–841. https://doi.org/10.5194/angeo-26-823-2008

Ding, F., Wan, W., Li, Q., Zhang, R., Song, Q., Ning, B., et al. (2014). Comparative climatological study of large-scale traveling ionospheric disturbances over North America and China in 2011–2012. *Journal of Geophysical Research: Space Physics*, *119*(1), 519–529. https://doi.org/10.1002/2013JA019523

Ding, F., Wan, W., Ning, B., & Wang, M. (2007). Large-scale traveling ionospheric disturbances observed by GPS total electron content during the magnetic storm of 29–30 October 2003. *Journal of Geophysical Research*, *112*(A6), A06309. https://doi.org/10.1029/2006JA012013

Fejer, B. G. (2002). Low latitude storm time ionospheric electrodynamics. *Journal of Atmospheric and Solar-Terrestrial Physics*, *64*(12–14), 1401–1408. https://doi.org/10.1016/S1364-6826(02)00103-7

Figueiredo, C. A. O. B., Wrasse, C. M., Takahashi, H., Otsuka, Y., Shiokawa, K., & Barros, D. (2017). Large-scale traveling ionospheric disturbances observed by GPS dTEC maps over North and South America on Saint Patrick's Day storm in 2015. *Journal of Geophysical Research: Space Physics*, *122*(4), 4755–4763. https://doi.org/10.1002/2016JA023417

Guerra, M., Cesaroni, C., Ravanelli, M., & Spogli, L. (2024). Travelling ionospheric disturbances detection: A statistical study of detrending techniques, induced period error and near real-time observables. *J. Space Weather Space Clim.*, *14*, 17. https://doi.org/10.1051/swsc/2024017

Guo, X., Zhao, B., Yu, T., Hao, H., Sun, W., Wang, G., et al. (2024). East–west difference in the ionospheric response during the recovery phase of May 2024 super geomagnetic storm over the East Asian. *Journal of Geophysical Research: Space Physics*, *129*(9), e2024JA033170. https://doi.org/10.1029/2024JA033170

Habarulema, J. B., Yizengaw, E., Katamzi-Joseph, Z. T., Moldwin, M. B., & Buchert, S. (2018). Storm time global observations of large-scale TIDs from ground-based andin situ satellite measurements. *Journal of Geophysical Research: Space Physics*, *123*(1), 711–724. https://doi.org/10.1002/2017JA024510

Hao, H., Zhao, B., Jin, Y., Yue, X., Ding, F., Li, G., et al. (2024). Latitude variation of the post-sunset plasma density enhancement during the minor geomagnetic storm on 27 May 2021. *Journal of Geophysical Research: Space Physics*, *129*(3), e2023JA032156. https://doi.org/10.1029/2023JA032156

Hao, Y., Huang, J., Liu, W., Zhang, D., & Xiao, Z. (2017). Prompt GPS TEC response to magnetospheric compression. *Journal of Geophysical Research: Space Physics*, *122*(4), 4357–4366. https://doi.org/10.1002/2017JA023866

Hu, L., Li, G., Ning, B., Sun, W., Xie, H., Zhao, X., et al. (2024). Development of low latitude long range ionospheric radar for observing plasma bubble irregularities and preliminary results. *Journal of Geophysical Research: Space Physics*, *129*(3), e2023JA032099. https://doi.org/10.1029/2023JA032099

Huang, C.-S. (2008). Continuous penetration of the interplanetary electric field to the equatorial ionosphere over eight hours during intense geomagnetic storms. *Journal of Geophysical Research*, *113*(A11), A11305. https://doi.org/10.1029/2008JA013588

Huang, C.-S., Sazykin, S., Chau, J. L., Maruyama, N., & Kelley, M. C. (2007). Penetration electric fields: Efficiency and characteristic time scale. *Journal of Atmospheric and Solar-Terrestrial Physics*, *69*(10–11), 1135–1146. https://doi.org/10.1016/j.jastp.2006.08.06

Huang, F., Lei, J., & Dou, X. (2017). Daytime ionospheric longitudinal gradients seen in the observations from a regional BeiDou GEO receiver network. *Journal of Geophysical Research: Space Physics*, *122*(6), 6552–6561. https://doi.org/10.1002/2017JA023881

Huang, Y.-N., & Cheng, K. (1991). Ionospheric disturbances at the equatorial anomaly crest region during the March 1989 magnetic storms. *Journal of Geophysical Research*, *96*(A8), 13953–13965. https://doi.org/10.1029/91ja01086

Kelley, M. C., Makela, J. J., Chau, J. L., & Nicolls, M. J. (2003). Penetration of the solar wind electric field into the magnetosphere/ionosphere system. *Geophysical Research Letters*, *30*(4), 1158. https://doi.org/10.1029/2002GL016321

Kuai, J., Liu, L., Liu, J., Sripathi, S., Zhao, B., Chen, Y., et al. (2016). Effects of disturbed electric fields in the low latitude and equatorial ionosphere during the 2015 St. Patrick's Day storm. *Journal of Geophysical Research: Space Physics*, *121*(9), 9111–9126. https://doi.org/10.1002/2016JA022832

Kuai, J., Liu, L., Liu, J., Zhao, B., Chen, Y., Le, H., & Wan, W. (2015). The long-duration positive storm effects in the equatorial ionosphere over Jicamarca. *Journal of Geophysical Research: Space Physics*, *120*(2), 1311–1324. https://doi.org/10.1002/2014JA020552

Lei, J., Thayer, J. P., Lu, G., Burns, A. G., Wang, W., Sutton, E. K., & Emery, B. A. (2011). Rapid recovery of thermosphere density during the October 2003 geomagnetic storms. *Journal of Geophysical Research*, *116*(A3), A03306. https://doi.org/10.1029/2010JA016164

Li, G., Ning, B., Zhao, X., Sun, W., Hu, L., Xie, H., et al. (2019). Low latitude ionospheric TEC oscillations associated with periodic changes in IMF Bz polarity. *Geophysical Research Letters*, *46*(16), 9379–9387. https://doi.org/10.1029/2019GL084428

Liu, H., Ding, F., Zhao, B., Li, J., Hu, L., Wan, W., & Ning, B. (2017). Ionospheric response following the Mw 7.8 Gorkha earthquake on 25 April 2015. *Journal of Geophysical Research: Space Physics*, *122*(6), 6495–6507. https://doi.org/10.1002/2016JA023079

Liu, W., Blanc, M., Wang, C., Donavan, E., Foster, J., Lester, M., et al. (2021). Scientific challenges and instrumentation for the international meridian Circle Program. *Science China Earth Sciences*, *64*(12), 2090–2097. https://doi.org/10.1007/s11430-021-9841-8

Lu, G., Goncharenko, L. P., Richmond, A. D., Roble, R. G., & Aponte, N. (2008). A dayside ionospheric positive storm phase driven by neutral winds. *Journal of Geophysical Research*, *113*(A8), A08304. https://doi.org/10.1029/2007JA012895

Matzka, J., Stolle, C., Yamazaki, Y., Bronkalla, O., & Morschhauser, A. (2021). The geomagnetic Kp index and derived indices of geomagnetic activity. *Space Weather*, *19*(5), e2020SW002641. https://doi.org/10.1029/2020SW002641

Nava, B., Rodríguez-Zuluaga, J., Alazo-Cuartas, K., Kashcheyev, A., Migoya-Orué, Y., Radicella, S. M., et al. (2016). Middle- and low-latitude ionosphere response to 2015 St. Patrick's Day geomagnetic storm. *Journal of Geophysical Research: Space Physics*, *121*(4), 3421–3438. https://doi.org/10.1002/2015JA022299

Prölss, G. W. (1993). Common origin of positive ionospheric storms at middle latitudes and the geomagnetic activity effect at low latitudes. *Journal of Geophysical Research*, *98*(A4), 5981–5991. https://doi.org/10.1029/92JA02777

Prölss, G. W., & Werner, S. (2002). Vibrationally excited nitrogen and oxygen and the origin of negative ionospheric storms. *Journal of Geophysical Research*, *107*(A2), 1016. https://doi.org/10.1029/2001JA900126

Shiokawa, K., Otsuka, Y., Ogawa, T., Balan, N., Igarashi, K., Ridley, J., et al. (2002). A large-scale traveling ionospheric disturbance during the magnetic storm of 15 September 1999. *Journal of Geophysical Research*, *107*(A6), 1088. https://doi.org/10.1029/2001JA000245

Spogli, L., Alberti, T., Bagiacchi, P., Cafarella, L., Cesaroni, C., Cianchini, G., et al. (2024). The effects of the may 2024 Mother's day superstorm over the mediterranean sector: From data to public communication. *Annals of Geophysics*, *67*(2), PA218. https://doi.org/10.4401/ag-9117

Spogli, L., Sabbagh, D., Regi, M., Cesaroni, C., Perrone, L., Alfonsi, L., et al. (2021). Ionospheric response over Brazil to the August 2018 geomagnetic storm as probed by CSES-01 and Swarm satellites and by local ground-based observations. *Journal of Geophysical Research: Space Physics*, *126*(2), e2020JA028368. https://doi.org/10.1029/2020JA028368

Sun, W. (2024). Ionospheric data during the May 2024 super geomagnetic storm [Dataset]. https://doi.org/10.12197/2024GA014

Sun, W., Li, G., Le, H., Chen, Y., Hu, L., Yang, S., et al. (2022). Daytime ionospheric large-scale plasma density depletion structures detected at low latitudes under relatively quiet geomagnetic conditions. *Journal of Geophysical Research: Space Physics*, *127*(2), e2021JA030033. https://doi.org/10.1029/2021JA030033

Sun, W., Li, G., Ning, B., Hu, L., Otsuka, Y., Dai, G., et al. (2024). Monitoring of ionospheric variability using the Low lAtitude long Range Ionospheric raDar (LARID): Capabilities, advantages and limitations. *Space Weather*, *22*, e2024SW004134. https://doi.org/10.1029/2024SW004134

Sun, W., Li, G., Zhao, B., Zhang, S.-R., Otsuka, Y., Hu, L., et al. (2024). Midlatitude plasma blob-like structures along with super equatorial plasma bubbles during the May 2024 great geomagnetic storm. *Geophysical Research Letters*, *51*, e2024GL111638. https://doi.org/10.1029/2024GL111638

Sun, W., Wu, B., Wu, Z., Hu, L., Zhao, X., Zheng, J., et al. (2020). Ionise: An ionospheric observational network for irregularity and scintillation in East and Southeast Asia. *Journal of Geophysical Research: Space Physics*, *125*(8), e2020JA028055. https://doi.org/10.1029/2020JA028055

Wang, C. (2010). New chains of space weather monitoring stations in China. *Space Weather*, *8*, S08001. https://doi.org/10.1029/2010SW000603

Wang, C., Xu, J., Liu, L., Xue, X., Zhang, Q., Hao, Y., et al., (2023). Contribution of the Chinese Meridian Project to space environment research: Highlights and perspectives. *Science China Earth Sciences*, *66*(7), 1423–1438. https://doi.org/10.1007/s11430-022-1043-3

Wanliss, J. A., & Showalter, K. M. (2006). High-resolution global storm index: DST versus SYM-H. *Journal of Geophysical Research*, *111*(A2), A02202. https://doi.org/10.1029/2005JA011034

Wei, Y., Zhao, B., Li, G., & Wan, W. (2015). Electric field penetration into Earth's ionosphere: A brief review for 2000-2013. *Science Bulletin*, *60*(8), 748–761. https://doi.org/10.1007/s11434-015-0749-4

Xiong, B., Wan, W., Yu, Y., & Hu, L. (2016). Investigation of ionospheric TEC over China based on GNSS data. *Advances in Space Research*, *58*(6), 867–877. https://doi.org/10.1016/j.asr.2016.05.033

Xiong, B., Wang, Y., Li, Y., Zhao, B., Yu, Y., Ren, Z., et al. (2023). Anomalous disturbance of the ionosphere in the East Asia region during the geomagnetically quiet day on 1 November 2016. *Journal of Geophysical Research: Space Physics*, *128*(2), e2022JA030905. https://doi.org/10.1029/2022JA030905

Zakharenkova, I., Astafyeva, E., & Cherniak, I. (2016). GPS and GLONASS observations of large-scale traveling ionospheric disturbances during the 2015 St. Patrick's Day storm. *Journal of Geophysical Research: Space Physics*, *121*(12), 138–212. https://doi.org/10.1002/2016JA023332

Zhang, S.-R., Nishimura, Y., Vierinen, J., Lyons, L. R., Knipp, D. J., Gustavsson, B. J., et al. (2023). Simultaneous global ionospheric disturbances associated with penetration electric fields during intense and minor solar and geomagnetic disturbances. *Geophysical Research Letters*, *50*(19), e2023GL104250. https://doi.org/10.1029/2023GL104250

Zhang, S.-R., Zhang, Y., Wang, W., & Verkhoglyadova, O. P. (2017). Geospace system responses to the St. Patrick's Day storms in 2013 and 2015. *Journal of Geophysical Research: Space Physics*, *122*(6), 6901–6906. https://doi.org/10.1002/2017JA024232

Zhao, B., Wan, W., Lei, J., Wei, Y., Sahai, Y., & Reinisch, B. (2012). Positive ionospheric storm effects at Latin America longitude during the superstorm of 20–22 November 2003: Revisit. *Annals of Geophysics*, *30*(5), 831–840. https://doi.org/10.5194/angeo-30-831-2012

Zhao, B., Wan, W., Tschu, K., Igarashi, K., Kikuchi, T., Nozaki, K., et al. (2008). Ionosphere disturbances observed throughout Southeast Asia of the superstorm of 20–22 November 2003. *Journal of Geophysical Research*, *113*(A3), A00A04. https://doi.org/10.1029/2008JA013054

Zhao, B., Yang, C., Cai, Y., Jin, Y., Liang, Y., Ding, F., et al. (2019). East-west difference in the ionospheric response of the March 1989 great magnetic storm throughout East Asian region. *Journal of Geophysical Research: Space Physics*, *124*(11), 9364–9380. https://doi.org/10.1029/2019JA027108